Understanding and Controlling the Weld Microstructure of Steels

The analysis of microstructure development in steel weld metals is addressed

BY T. KOSEKI

Abstract

In this article, selected studies are reviewed with a focus on the analysis of microstructure development in steel weld metals. In the study of austenitic stainless steel weld metals, microstructure development in the primary ferrite solidification mode (FA mode) was clarified and related to why FA-mode welds are resistant to hot cracking. In studies of duplex stainless steel weld metals and high-Cr ferritic stainless steel weld metals, nitrogen-driven microstructure development and TiN-assisted grain refinement, respectively, were described, and discussions about the mechanism of equiaxed grain formation in the weld metals were added in the latter. In the study of low-alloy steel weld metals, the roles of titanium oxide and titanium nitride (TiN) inclusions on intragranular ferrite formation and the refinement of weld microstructure were described based on crystallographic analysis and the first principles calculation. At the end, the potential importance of the application of different multiscale, multiphysics simulations to welding research was pointed out.

Keywords

Introduction

It was a great pleasure to receive the 2022 Comfort A. Adams Lecture Award and to be given this opportunity to present a review article about my welding research for the *Welding Journal*. Over the past 40 years, I have been involved in various research projects on the welding of different steels. The major research interest has been understanding microstructure development during welding because it is always critical to achieving the desired properties and performances of weld metals.

When I started my research on the weldability of stainless steels in the 1980s, research on the solidification and microstructure of austenitic stainless steel weld metals was actively being driven by pioneering studies conducted in the late '70s to early '80s (Refs. 1–10). Classification of the solidification mode and microstructure, prediction of the solidification mode and ferrite content, and the effect of the mode and microstructure on weld performance, such as hot-cracking susceptibility, corrosion resistance, and cryogenic toughness, were investigated by pioneering studies; those studies were expanded by subsequent studies for better understanding. My initial work (Refs. 11, 18) was among the subsequent studies being stimulated by the pioneering studies.

In this context, this article starts with reviewing my research on the solidification and microstructure of austenitic stainless steel weld metals, and then the review is extended to those of duplex and ferritic stainless steel and low-alloy steel weld metals. The main focus is placed on the mechanism of microstructure development in those welds and also on how weld microstructure can be controlled. At the end, some comments are added regarding a future direction of welding research based on my research activities and recent research trends.
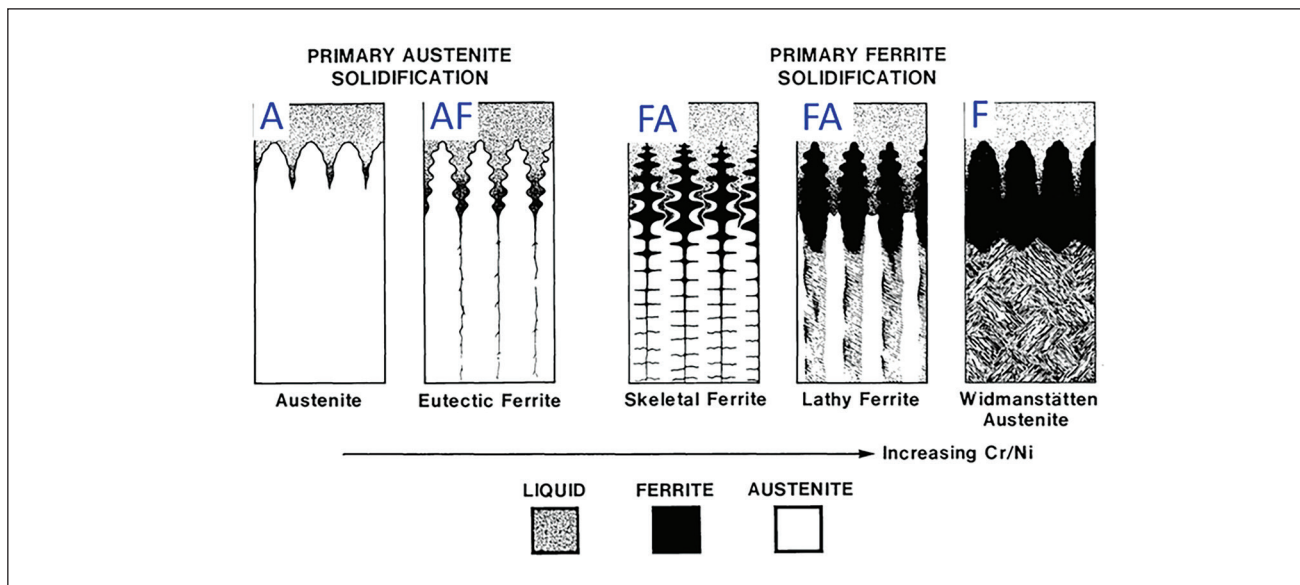
Fig. 1 — Schematic presentation of the solidification mode of austenitic stainless steel weld metals by Brooks and Thompson (Ref. 12). Note: Modes A, AF, FA, and F were added to the original by the author.

Hot-Cracking Susceptibility of FA-Mode Austenitic Stainless Steel Weld Metals

The solidification of austenitic stainless steel weld metals is classified into four modes, A, AF, FA, and F, which are schematically summarized in Fig. 1, presented by Brooks and Thompson (Ref. 12). Both the A and AF modes start with the primary phase of austenite. A completes as austenite single phase, but AF completes with the formation of ferrite in the last stage of solidification in the interdendritic region by eutectic reaction. In FA mode, solidification starts with a primary ferrite, and austenite subsequently forms in the course of solidification by either a peritectic or eutectic reaction. The primary ferrite partially transforms to austenite during solidification and postsolidification cooling, which results in retained ferrite at the core of dendrites with different morphologies in the final microstructure, as depicted in Fig. 1. In F mode, solidification starts and completes as ferrite, and austenite subsequently forms from the ferrite grain boundaries during postsolidification cooling.

Among the four solidification modes of austenitic stainless steel weld metals, FA mode is the most complicated, and, thus, its microstructure development has been examined by many researchers (Refs. 12, 13). On the other hand, FA mode is practically important, offering much lower hot-cracking susceptibility over the A and AF modes (as seen in Fig. 2 by Kujanpaa et al. [Ref. 14]), which has led to the fact that many welding consumables for welding austenitic stainless steels are alloy designed so the welds can solidify with FA mode. Brooks and Thompson (Refs. 12, 13) suggested the following three reasons FA mode offers low hot-cracking susceptibility:

1. Irregular grain boundaries, resulting in a more-complicated crack

2. Lower surface energies of ferrite/austenite boundaries that prevent the boundary from being wetted by impurity containing liquid
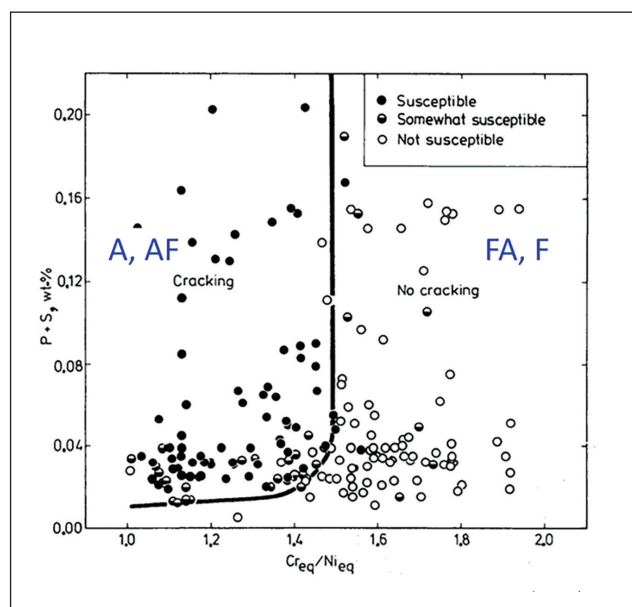

Fig. 2 — Effect of solidification mode and impurities (P + S) on weld hot-cracking susceptibility (Ref. 14). Note: Modes A, AF, FA, and F were added to the original by the author.

3. Increased solubility of impurities in ferrite that reduces the amount of the low-melting impurity-containing phase.

The understanding of FA mode is important not only for the understanding of fundamental weld behavior but also for the practical alloy design of welding materials. The author and his colleagues were also interested in and worked on this issue (Refs. 15, 16) with a particular emphasis on crystallographic analysis of FA-mode welds that had not been conducted sufficiently.
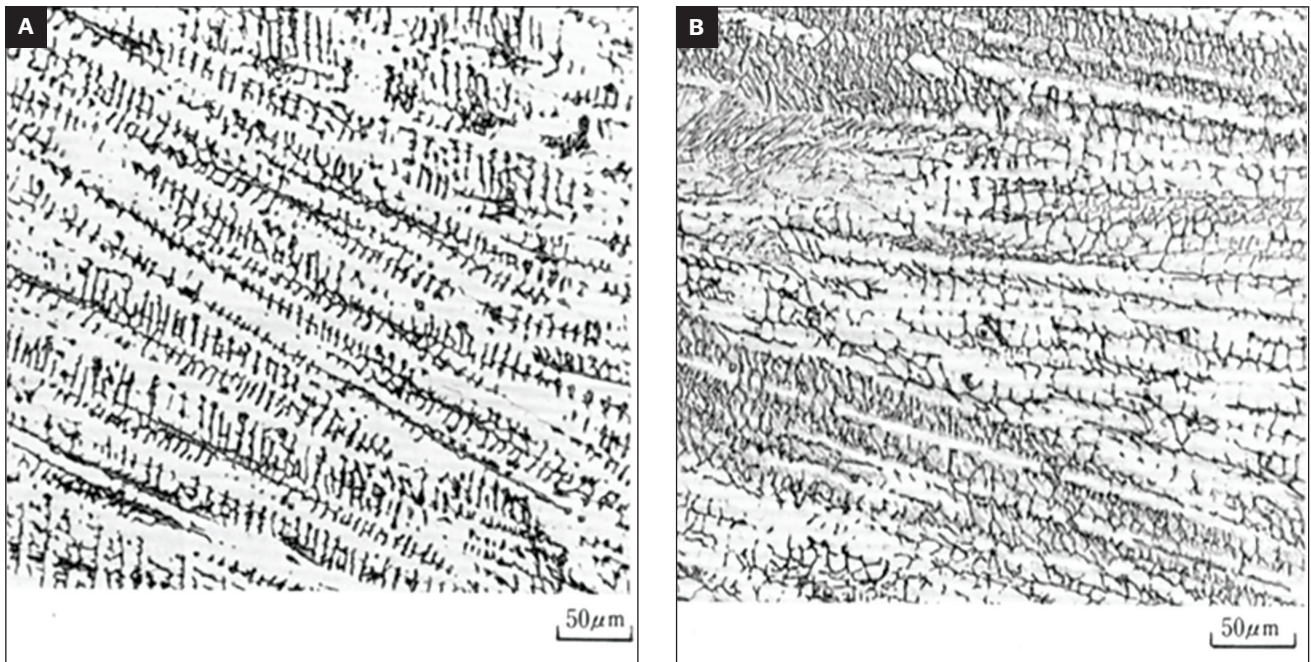
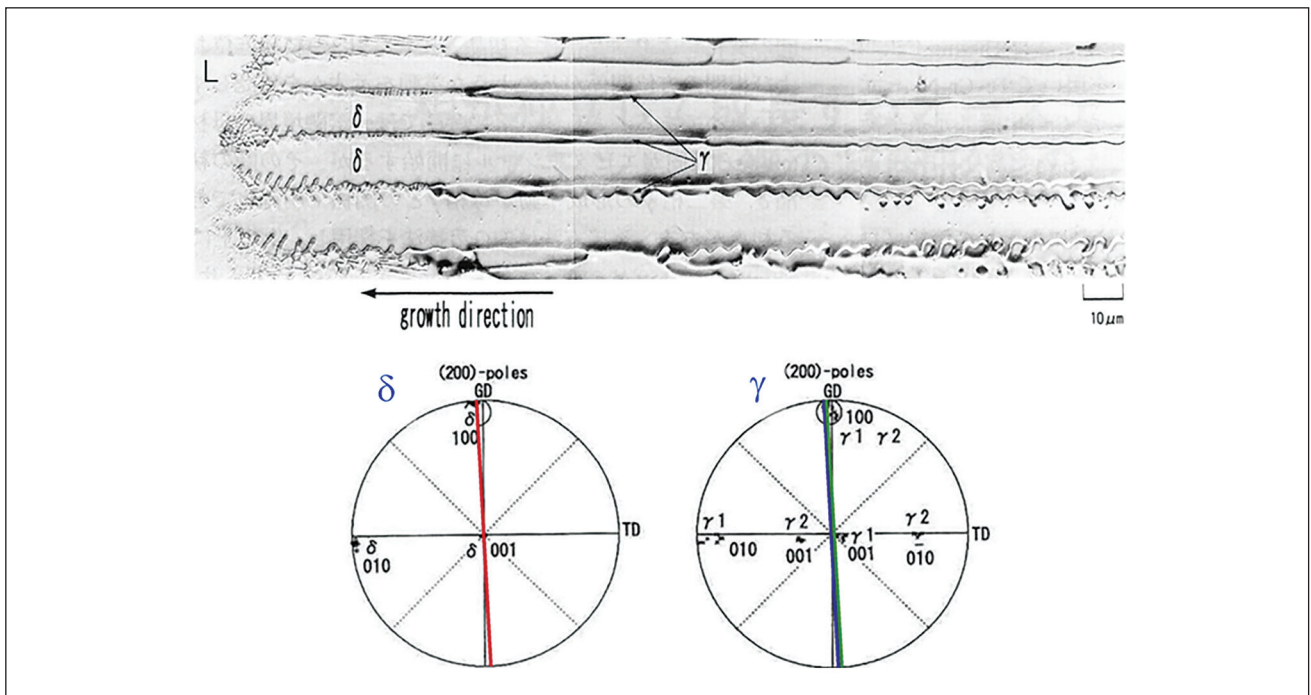Fig. 3 — Microstructure of the FA-mode weld metals. A — Skeletal or vermicular ferrite; B — lacy ferrite.

Fig. 4 — Solidification front of a FA-mode (19 wt-% Cr-11 wt-% Ni) stainless steel weld obtained by quenching the weld pool using liquid tin during welding, along with pole figures of primary ferrite (δ) and interdendrite austenite (γ) (Ref. 16).

An important result from the crystallographic analysis of FA-mode welds is that there is usually a parallel relationship between <100> of ferrite and <100> of austenite in FA-mode welds. Figure 3 shows two typical microstructures of FA-mode welds having different ferrite morphologies, where dark (black) is ferrite and bright (white) is austenite matrix, along with pole figures of the phases. A common feature of the two FA-mode welds is the parallel relationship between <100> of ferrite and <100> of austenite. To examine where this parallel relationship starts, the solidification front of a FA-mode weld was observed by quenching the weld pool using liquid tin during welding. The microstructure of the
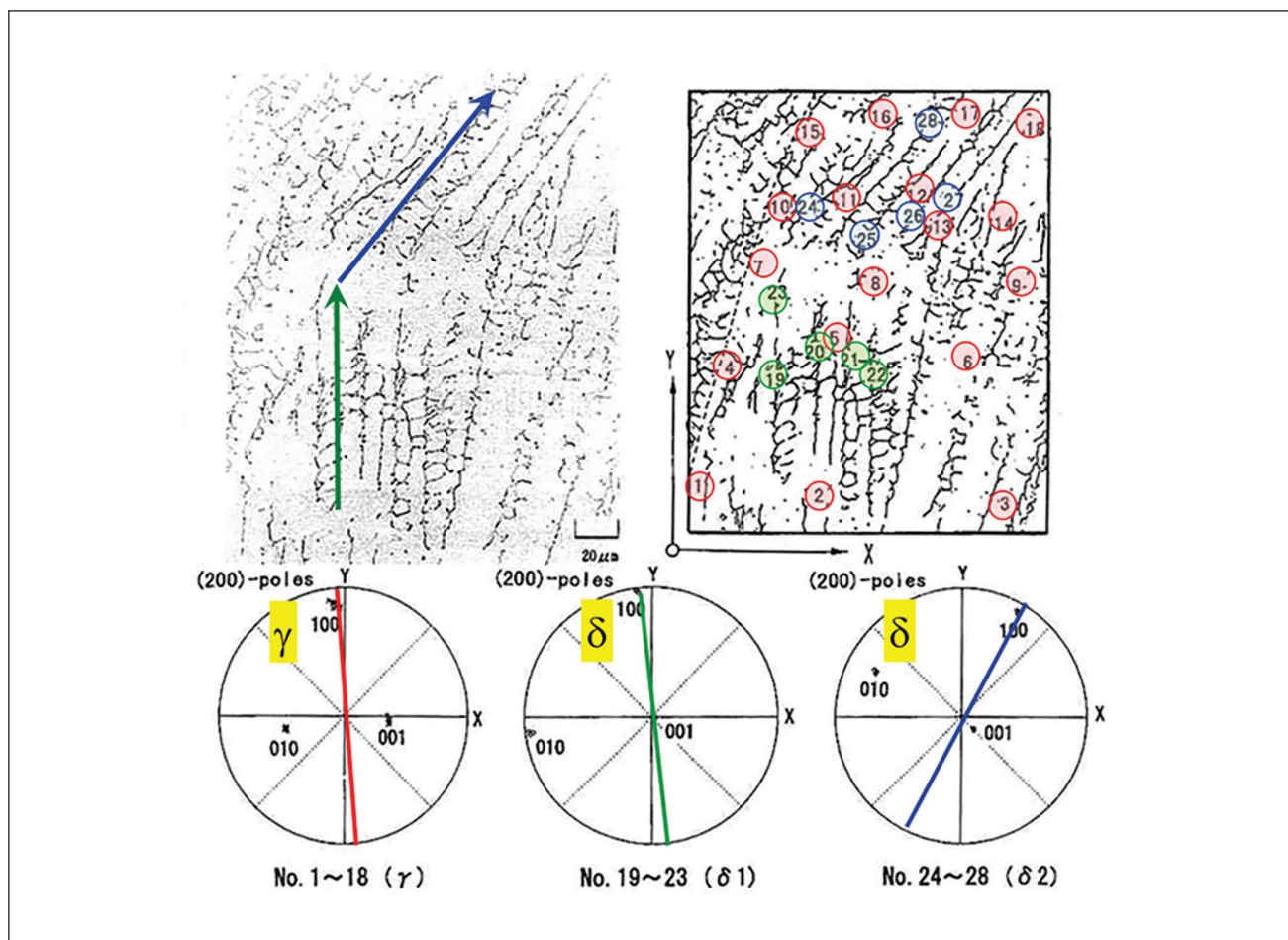
Fig. 5 — Optical microstructure of a FA-mode (19 wt-% Cr-11 wt-% Ni) stainless steel weld and pole figures from ferrite (δ, black) and austenite (γ, white), where ferrite grows upward from the bottom and changes growth direction in the middle (as shown with green to blue) while austenite is matrix (as shown with red) (Ref. 16).

weld is shown in Fig. 4 (Ref. 16), along with pole figures of the phases. Ferrite dendrites grow into the liquid (i.e., weld pool) from the right to left of the figure, which is parallel to the heat flow from left to right, and the crystallographic growth direction of the ferrite is identified as <100>, the preferential growth direction for the solidification of the body-centered cubic (bcc). At the same time, in the interdendritic regions, austenite is observed to grow as if independently, and the growth direction is identified as <100>, the preferential growth direction for the solidification of the face-centered cubic (fcc). Therefore, it was concluded that the parallel relationship between <100> of ferrite and <100> of austenite in FA-mode welds originally comes from the solidification stage, and this seems to indicate that, in FA-mode solidification, ferrite and austenite grow independently, each growing with its preferential growth direction without any restriction on each other.

The next question is whether the parallel relationship between <100> of ferrite and <100> of austenite is continued when the growth direction is changed by the change of heat flow direction with a moving heat source. Figure 5 (Ref. 16) shows a region in which the growth direction of ferrite changes. Skeletal ferrite (black) indicates that it grows

upward from the bottom to the middle of the figure, and then the growth direction changes to right upward, both of which are also confirmed by the change of <100> direction in the pole figures attached. On the other hand, as the pole figure for austenite suggests, it seems that austenite (white) continuously grows upward from the bottom to the top of the figure even after ferrite changes the growth direction in the middle. This supports the idea that ferrite and austenite grow independently and indicates that the change of growth direction of ferrite does not occur at the same time as that of austenite.

The independent growth of ferrite and austenite is more clearly verified when multiple grains are evaluated by electron backscatter diffraction (EBSD), as shown in Fig. 6 (Ref. 16), where the optical microstructure of the observed area is shown in A and the corresponding EBSD phase mapping for ferrite and austenite are shown in B and C, respectively. It should be noted that the same orientation area results in the same color in each mapping. From ferrite morphology in A and the corresponding color of ferrite in B, ferrite grain boundaries are indicated by the dotted lines added in A. However, the austenite grain boundaries identified in C do not match the ferrite boundaries, and, moreover, they are not
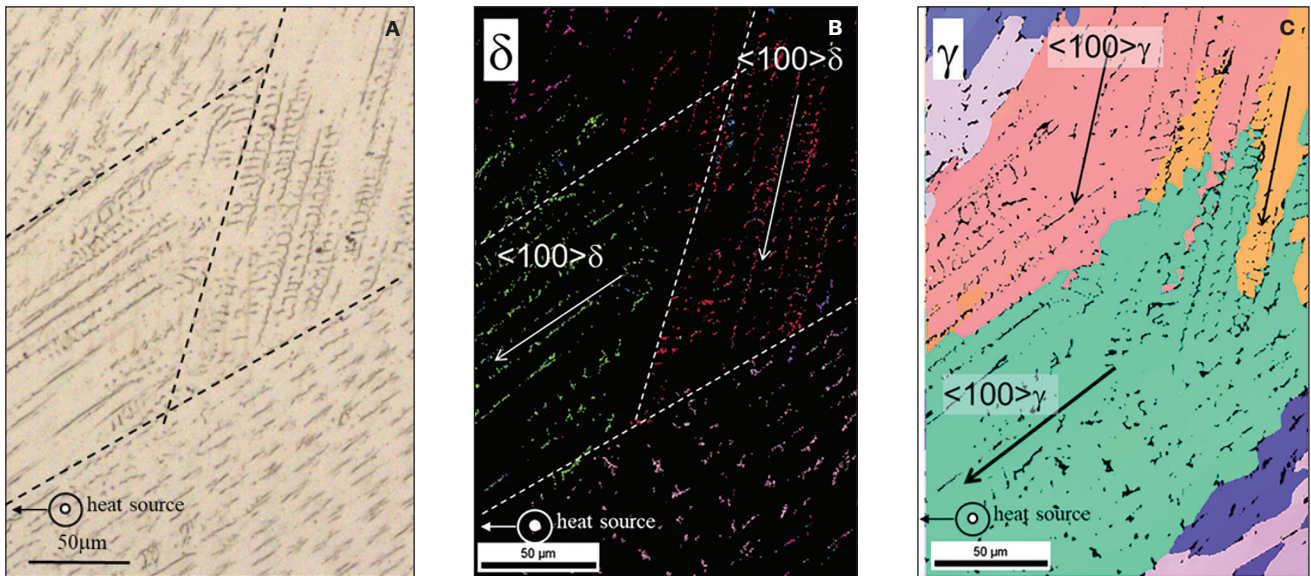
Fig. 6 — A — Optical microstructure of a FA-mode (19 wt-% Cr-11 wt-% Ni) stainless steel weld; B, C — EBSD phase mapping of ferrite (δ) and austenite (γ), where ferrite and austenite grow downward from the top and change growth direction in the middle (as shown with arrows). Note: Arrows and borders with dotted lines were added to the original figure from Ref. 16 for clarification.
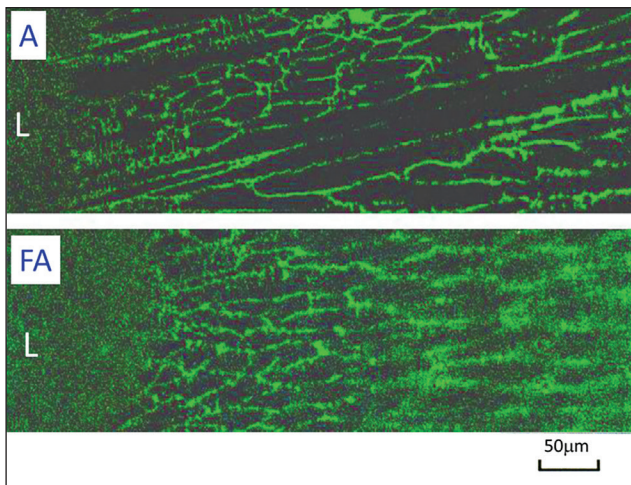

Fig. 7 — Phosphorus distribution at the solidification front in A-mode and FA-mode welds.

smooth or straight but rather irregular. This suggests that the grain structure developments of ferrite and austenite are independent of each other, as considered in the previous figure. In addition, the irregular boundaries seem to result from the pinning of austenite solidification growth by preexisting primary ferrite. Because the final part of solidification is along austenite grain boundaries, the irregular austenite boundaries could lead to discontinuous remnant liquid in the last stage of solidification.

It seems that these observations confirm the above-mentioned reason number 1 suggested by Brooks and Thompson (irregular grain boundaries, resulting in a more-complicated crack) for the low cracking susceptibility of the FA-mode. Brooks and Thompson (Ref. 12) reported that while hot cracks in A-mode welds were long and extended along grain boundaries, those in FA-mode welds were short and blunt even in the Varestraint test, which should be the result from irregular austenite grain boundaries in the FA mode. It is said that hot-cracking susceptibility increases again when the solidification mode changes from FA to F, fully ferritic solidification (Ref. 17), although the level of susceptibility is low as compared with those of the A and AF modes. This can also be rationalized by the irregular austenite boundaries achieved by the two-phase independent solidification in the FA mode.

The other reasons number 2 and 3, proposed by Brooks and Thompson (Ref. 12), should not be ruled out, but it seems that they offer additional benefits to the first reason. Hot cracking in FA-mode welds should take place at austenite-austenite boundaries, the last part to solidify with low-melting-point liquid, and, thus, low interfacial energy between ferrite and austenite may not be the primary reason for low hot-cracking susceptibility. The third reason should lead to decreased segregation of impurity elements, such as phosphorus and sulfur, and thereby to reduced cracking susceptibility. Figure 7 (Ref. 18) compares the distribution of phosphorous at the solidification front of A-mode and FA-mode welds, both being obtained by the liquid-tin quenching during welding. Phosphorous is rejected to and enriched in the interdendritic regions in A-mode solidification, while the enrichment of phosphorous immediately becomes indistinct behind the solidification front due to rapid diffusion in FA-mode solidification. This significant back diffusion should be helpful in reducing phosphorus concentration at the last part to solidify, thus reducing the occurrence of cracking there. However, as seen in Fig. 2 (Ref. 14), low cracking susceptibility in FA mode is still held even with increasing impurity levels, which implies that high solubility and diffusivity of impurity elements in ferrite could not be the primary reason for low cracking susceptibility. Therefore, the irregular solidification grain
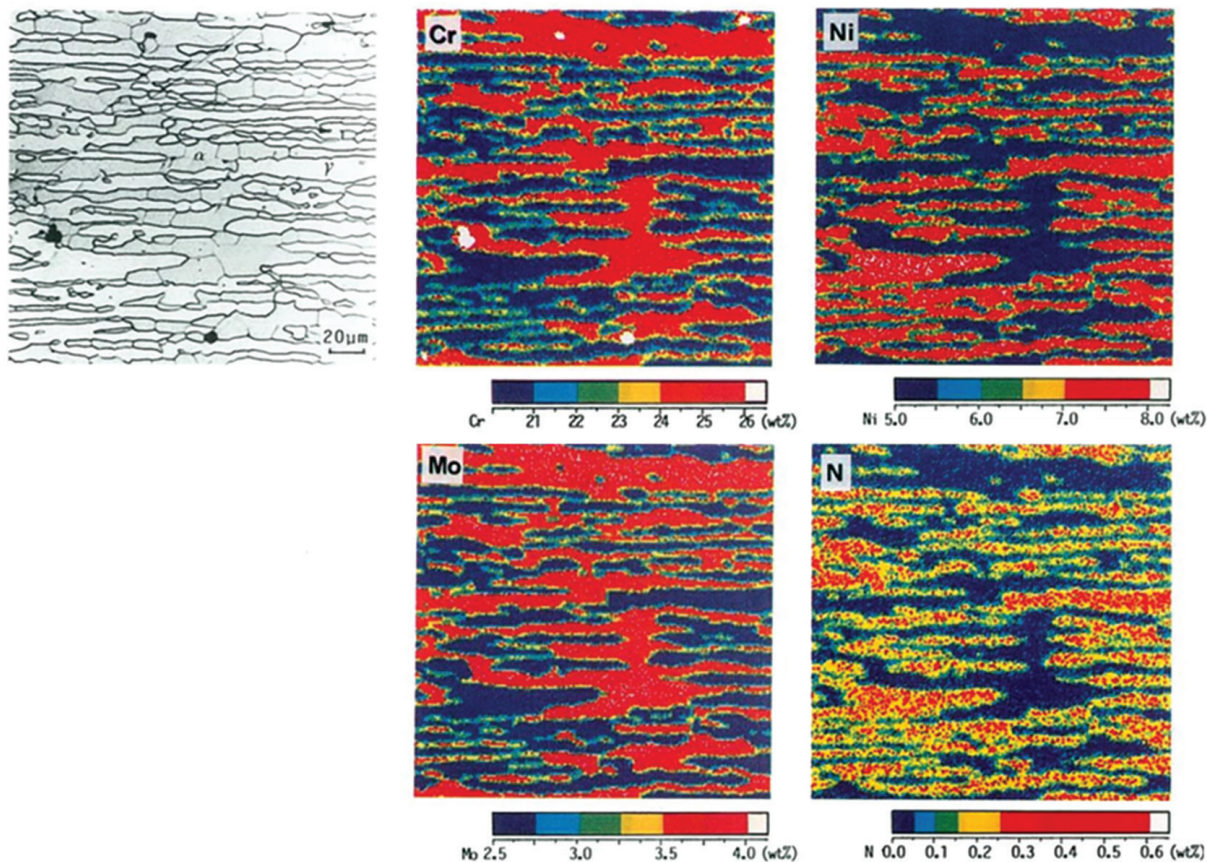
Fig. 8 — Microstructure and distribution of Cr, Ni, Mo, and N in a 22 wt-% Cr-6 wt-% Ni-3 wt-% Mo-0.12 wt-% N duplex stainless steel base metal (Ref. 20). It is noted the figures are all in monochrome in Ref. 20, but the original color results are shown here.

boundaries we confirmed in an investigation by the author and his colleagues (Refs. 15, 16) should be the primary reason for the low cracking susceptibility of FA-mode welds.

Ferrite-to-Austenite Transformation in F-Mode Duplex Stainless Steel Weld Metals

The solidification of duplex stainless steel welds corresponds to the F-mode (Fig. 1), which completes with the ferrite single phase, and austenite is subsequently formed in the solid state from the ferrite grain boundaries during postsolidification cooling (Ref. 19). The phase balance between ferrite and austenite in duplex stainless steels is usually kept equal to achieve good combinations of corrosion resistance and mechanical properties, but the austenite content decreases when duplex stainless steels are welded without filler metals. This is because the ferrite-to-austenite transformation is suppressed during relatively rapid postsolidification cooling in the weld, which leads to lower performance of the welds than that of base metals.

It was found by the author and his colleague (Ref. 20) that ferrite-to-austenite transformation is controlled by nitrogen,

and increasing nitrogen content is the key to the improvement of weld microstructure and performance. Figures 8 and 9 (Ref. 20) show the microstructure and the distribution of Cr, Ni, Mo, and N in the base metal and its autogenous gas tungsten arc weld metal of a duplex stainless steel containing 22 wt-% Cr, 6 wt-% Ni, 3 wt-% Mo, and 0.12 wt-% N. In the base metal, the microstructure was a so-called microduplex structure consisting of alternately layered ferrite and austenite. Ferrite-forming elements Cr and Mo were enriched in ferrite, and austenite-forming elements Ni and N were enriched in austenite. In the weld metal, on the other hand, the microduplex structure of the base metal was destroyed by remelting and solidification, and the microstructure consisted of coarse ferrite grains with allotriomorphic or Widmansttaten austenite along the grain boundaries. Nitrogen was significantly enriched in austenite, while the partitioning of Cr, Ni, and Mo between ferrite and austenite was not identified clearly. Also, N content was depleted in the vicinity of austenite. It was concluded that the austenite formation is controlled and stabilized by N in N-bearing duplex stainless steel weld metals, and the depletion of N in the vicinity of austenite indicates that the transformation to austenite is controlled by N diffusion. It was also noted that segregation of Ni is
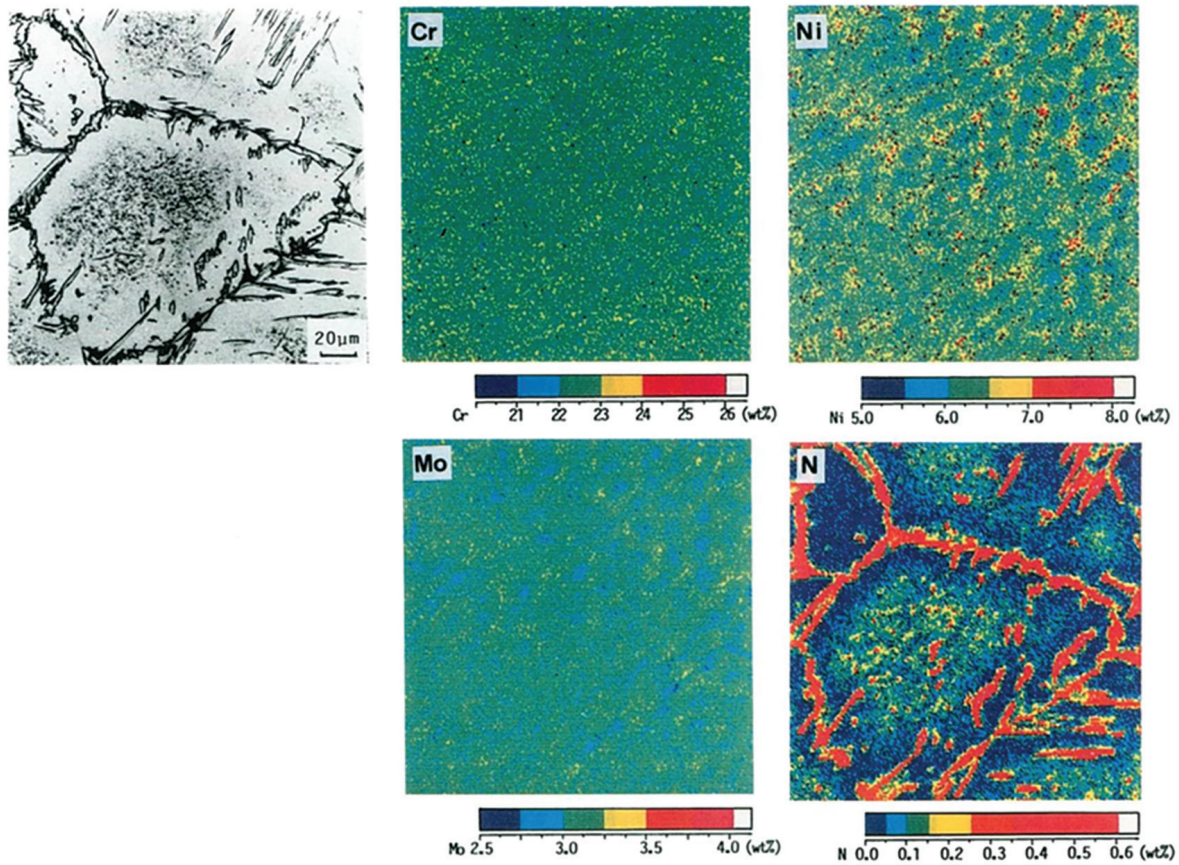
Fig. 9 — Microstructure and distribution of Cr, Ni, Mo, and N of a 22 wt-% Cr-6 wt-% Ni-3 wt-% Mo-0.12 wt-% N duplex stainless steel autogenous GTA weld (Ref. 20). It is noted the figures are all in monochrome in Ref. 20, but the original color results are shown here.
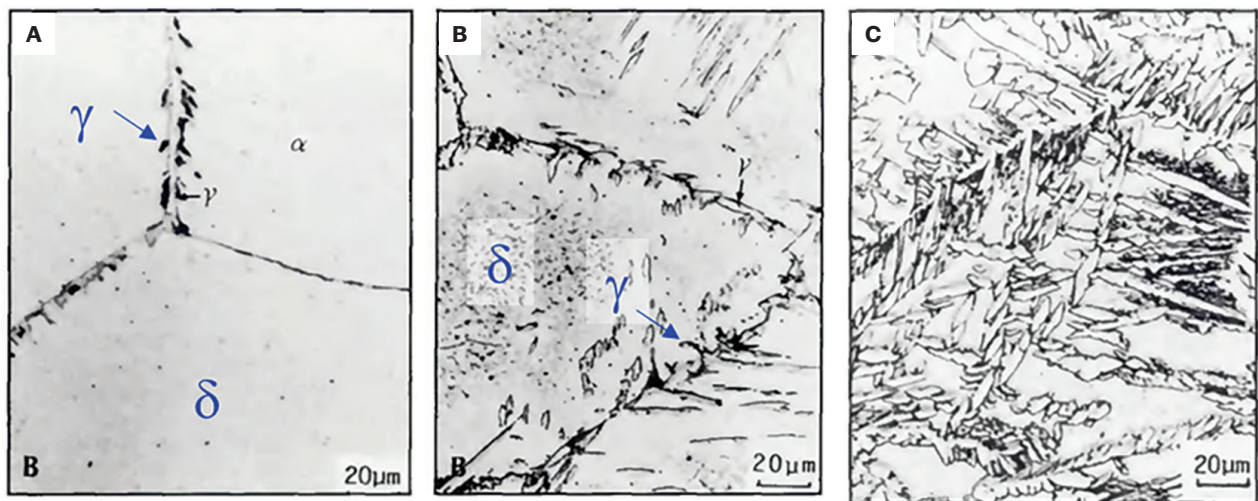

Fig. 10 — Microstructure of duplex stainless steel welds having different Ni and nitrogen contents. A — 22 Cr-9 Ni-3 Mo-0.03 N; B — 22 Cr-6 Ni-3 Mo-0.12 N (almost the same Ni equivalent as A); C — 22 Cr-6 Ni-3 Mo-0.18 N (Ref. 20).
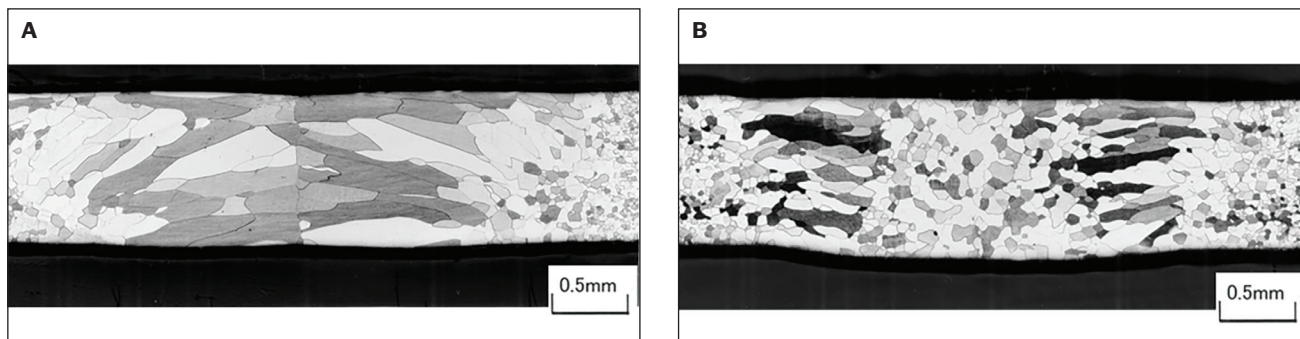
Fig. 11 — Microstructure of high-Cr ferritic stainless steel GTA welds having an alloy composition of: A — 17 wt-% Cr-0.007 wt-% Ti-0.0097 wt-% N; B — 17 wt-% Cr-0.3 wt-% Ti-0.0092 wt-% N (Ref. 22).
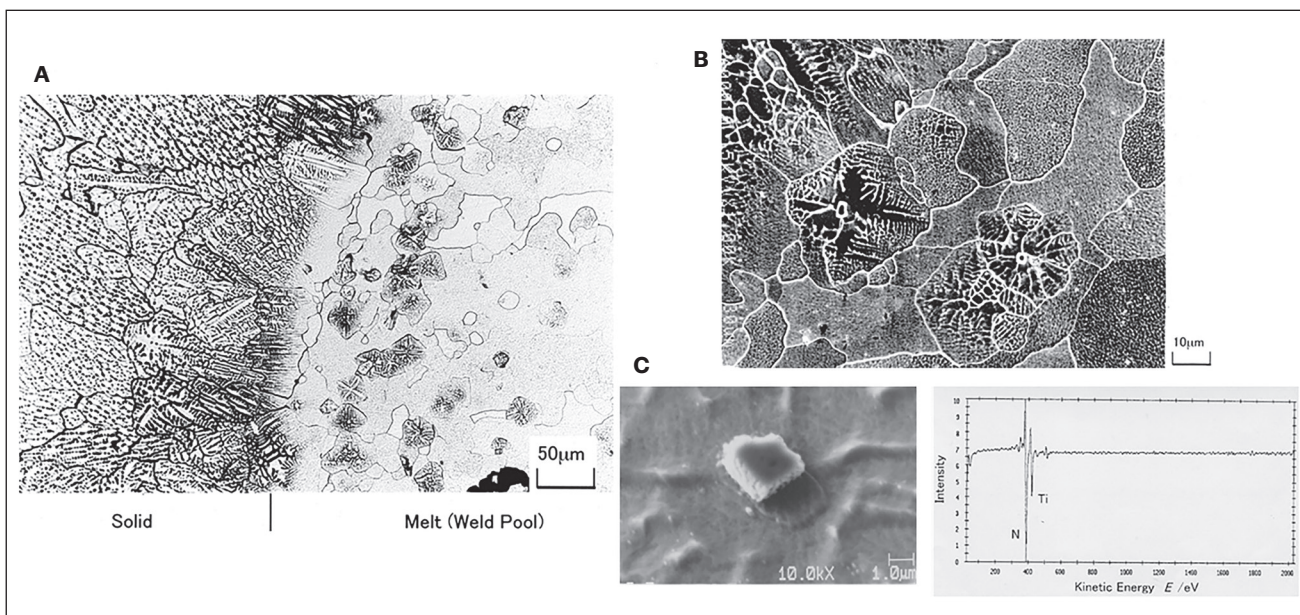

Fig. 12 — A — Solidification front of 17 Cr-0.3 Ti-0.0092 N ferritic stainless steel weld metal, obtained by the liquid-tin quenching of the weld pool during welding; B — equiaxed grain formation observed in the pool ahead of the solidification front; C — TiN at the center of the equiaxed grain and its AES analysis (Ref. 22).

seen in ferrite in the weld metal in Fig. 9. Nickel is probably enriched in interdendritic regions of ferrite solidification, but Ni enrichment does not affect austenite formation as an austenite former, which also supports the idea that N is more influential to austenite formation. Those measurements and analyses were reported for the first time in the research of duplex stainless steels by the author and his colleague in the *Welding Journal* (Ref. 20), where the measurement results could not be published in color but in monochrome; thus, in this article, the originals are shown in color.

Figure 10 (Ref. 20) demonstrates the beneficial effect of N on austenite formation in duplex stainless steel welds. Figures 10A and B compare the microstructure of two welds having compositions of 22% Cr-3% Mo-9% Ni-0.03% N and 22% Cr-3% Mo-6% Ni-0.12% N, respectively. They contain different amounts of Ni and N, but their Ni equivalents are almost identical; austenite formation from the ferrite grain boundaries is more obvious in the N-enriched weld, which confirms the effect of N. Rapid diffusion and redistribution of

N help austenite formation even during rapid postsolidification cooling of welds, while slow diffusion and redistribution of Ni does not work effectively. Figure 10C shows the microstructure of the weld containing 0.18% N, indicating further increase of austenite content over the 0.12% N-containing weld in Fig. 10B. The increase of austenite content and the improvement of ferrite-austenite balance improve the toughness and ductility of welds and corrosion resistance. In this context, most filler materials for the welding of duplex stainless steels are so designed that the weld deposits contain high N content.

Grain Refinement of F-Mode Ferritic Stainless Steel Weld Metals

High-chromium ferritic stainless steels solidify with the ferritic single phase and complete without any subsequent phase transformation to austenite; hence, the final micro-
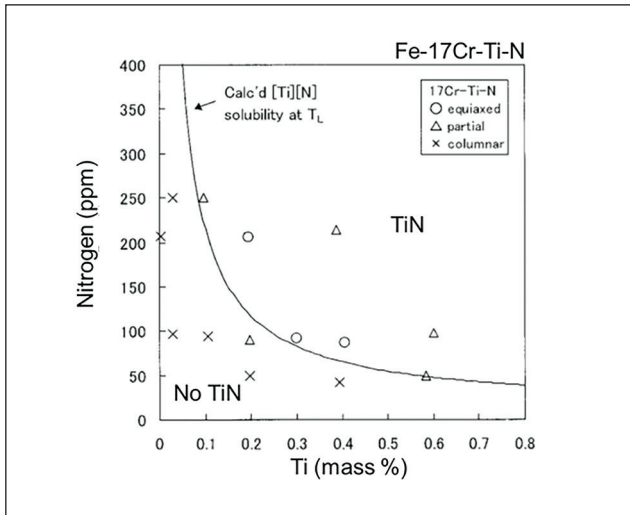
Fig. 13 — Solubility limit of titanium and nitrogen in 17 Cr steel calculated by Thermo-Calc, showing equiaxed grain formation is associated with TiN formation in the weld pool (Ref. 22).

Fig. 14 — A schematic of equiaxed grain formation in undercooled melt ahead of growing solid (dendrites) (Ref. 26).

structure consists of coarse, elongated ferrite grains growing from the fusion boundaries (Refs. 21–23), as shown in Fig. 11A (Ref. 22). Because this microstructure causes the degradation of toughness and ductility, the refinement of the weld microstructure was investigated and found to be achieved by the addition of titanium to welds (Refs. 21–23), as shown in Fig. 11B (Ref. 22). The author and his colleague investigated the mechanism of the refinement and clarified the equiaxed solidification in weld solidification.

By a liquid-tin quenching experiment, it was found that equiaxed grains form in the liquid just ahead of the solidification front, and titanium nitride (TiN) exists at the center of the grains, as shown in Fig. 12 (Ref. 22). TiN has a sodium chloride-type crystal structure and good lattice coherency with bcc-Fe when (100) and <100> of TiN are parallel to (100) and <110> of bcc-Fe, known as the Baker-Nutting (B-N) relationship (Ref. 24). Therefore, it is considered that TiN forming in the melt works as a nucleating agent for the equiaxed grains of ferrite. Figure 13 (Ref. 22) shows the solubility limit of Ti and N in Fe-17 mass% Cr melt at its liquidus temperature, which was calculated using Thermo-Calc (Ref. 25), and the experimental observation results of equiaxed grain formation are superposed in the figure. When the product of Ti and N contents is more than the solubility limit (i.e., higher content side of the solubility curve in the figure), TiN can precipitate in the melt; the contents of Ti and/or N become higher, and the formation temperature of TiN in the melt becomes greater. A comparison between the experimental observation of equiaxed grain formation and the solubility limit curve suggests that equiaxed grain formation is fortified when the contents of Ti and N are more than the solubility limit and close to the limit. It is inferred that the precipitation of TiN in the melt is a prerequisite for equiaxed grain formation, and TiN precipitation near the liquidus temperature of the steel (i.e., near the solidification front) is more effective to enhance equiaxed grains. This means that when the contents of Ti and N are much higher than the
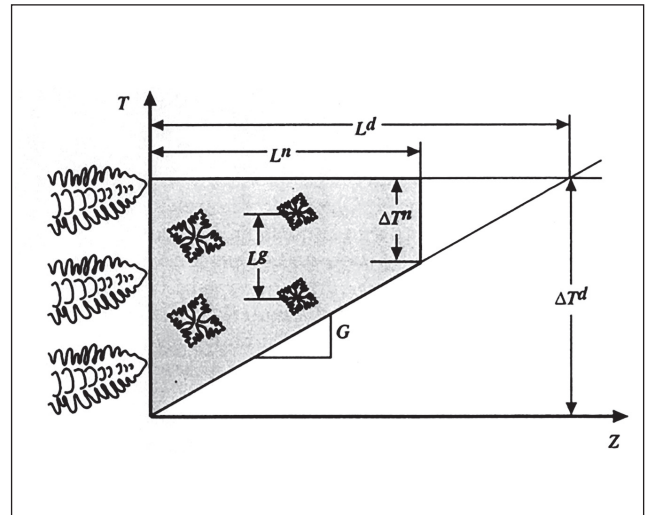
solubility limit, TiN precipitates at temperatures much higher than the liquidus temperature. Then TiN precipitates away from the solidification front and could grow by coarsening and ripening mechanisms, and the number of TiN supplied to the solidification front could decrease. In summary, it is clarified that the refining of the solidification microstructure in Ti-added high-Cr ferritic stainless steel welds is achieved by equiaxed solidification with a good nucleating agent, TiN, and the refinement is fortified when the Ti and N contents of steel are so designed as to lead to TiN precipitation at or slightly above the liquidus temperature of the steel.

Because weld solidification proceeds with a steep temperature gradient ahead of a growing solid, the possibility of equiaxed solidification is supposed to be quite limited in weld solidification unless high-potential nucleating agents are well supplied just in front of the growing solid in the weld pool, and in this case, the nucleating agent was confirmed as TiN. Figure 14 is a schematic of columnar-to-equiaxed transition (CET) by Gäumann and Kurz (Ref. 26), where ΔT_N and ΔT_d are the undercooling necessary for solid nucleation on the nucleating agent of interest and tip undercooling of dendritic growth, respectively. It is noted that tip undercooling, ΔT_d, is nearly equal to constitutional undercooling, ΔT_C, in welding, and ΔT_C can be calculated from steel chemistry and solidification condition. From Fig. 14, it is obviously inferred that if ΔT_d (i.e., ΔT_C) is greater than ΔT_N, the equiaxed grain can nucleate in the melt ahead of a growing solid. This situation was simulated by the author and his colleagues by using the Monte Carlo method, as shown in Fig. 15 (Ref. 23), where it was assumed that equiaxed grain can probabilistically nucleate with ΔT_N of 1.8 K on TiN dispersed randomly in the melt and the density of TiN was changed; details of the simulation are given elsewhere (Ref. 23). It is shown that columnar grains initially grow from the fusion boundary and undergo the transition to equiaxed grains in the middle in the presence of TiN, while the transition does not occur without TiN. The transition happens earlier and the number of equiaxed grains becomes larger as the number density of TiN
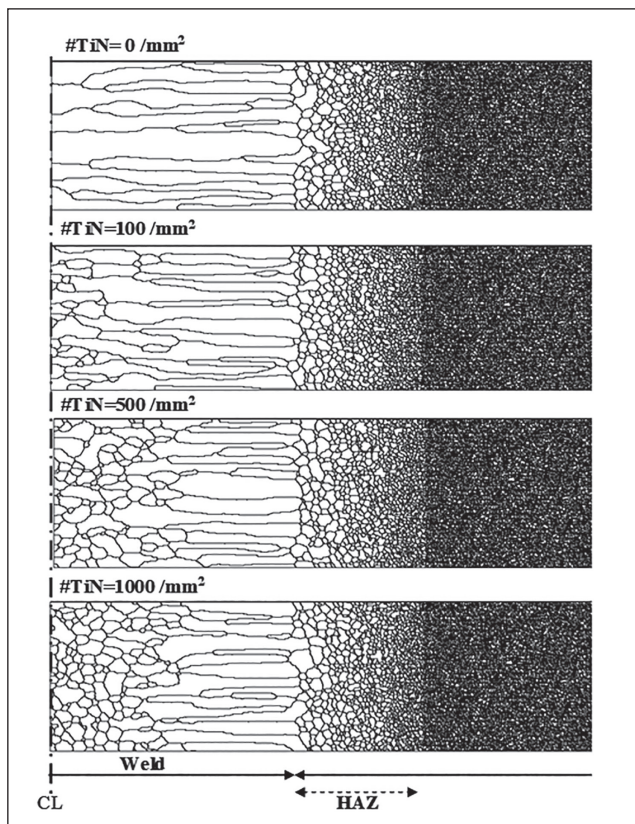
Fig. 15 — Monte Carlo simulation of the solidification of 17 Cr-0.4 Ti-N stainless steel weld containing different densities of TiN as a nucleating agent for equiaxed ferrite grain. Note that the solidification starts from the base metal of the right side and that ΔT_N is assumed to be 1.8 K (Ref. 23).
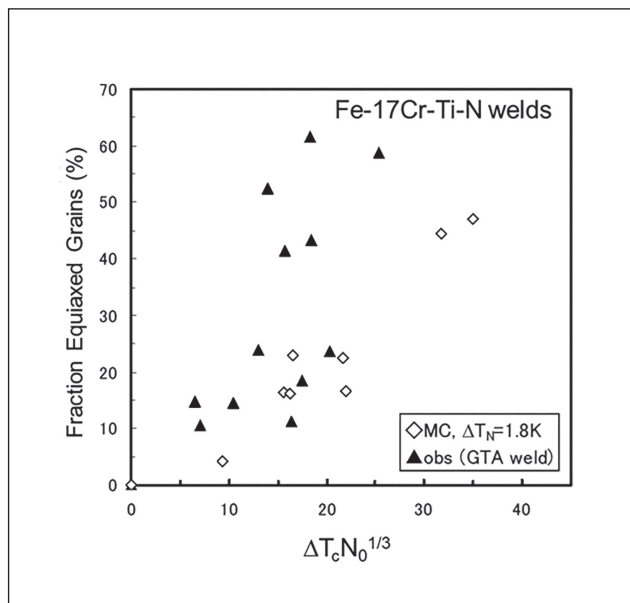

Fig. 16 — Relationship between $(N_0)^{1/3} \Delta T_C$ and the fraction of equiaxed grain area in weld metals obtained experimentally and from the Monte Carlo simulation (Ref. 23).

increases. According to the model proposed by Gäumann and Kurz (Ref. 26), CET takes place when the temperature gradient in liquid ahead of the growing solid, G, becomes:

$$G < a(N_0)^{\frac{1}{3}}\Delta T_C (1 - \frac{\Delta T_N}{\Delta T_C}) \qquad (1)$$

where N_0 is the number of nucleating sites of solid (i.e., the number of TiN in this case) and a is constant. The model means that CET is more likely as N_0 and ΔT_C increase and ΔT_N decreases. Figure 16 (Ref. 23) plots the relationship between $(N_0)^{1/3} \Delta T_C$ and the fraction of the equiaxed grain area in weld metals obtained experimentally and by a Monte Carlo simulation. The fraction of equiaxed grain area increases with increasing $(N_0)^{1/3} \Delta T_C$ in both experiments and simulations, and it was concluded that CET in welds occurs in accordance of the theoretical CET model (Ref. 26) when good nucleating agents offering sufficiently small ΔT_N are present in the weld pool.

Microstructure Refinement of Low-Alloy Steel Weld Metals

In the welding of low-alloy steels, refinement of the final microstructure is crucial to the toughness of the weld metal and the heat-affected zone (HAZ) of the base metal. The final ferritic and/or bainitic microstructure is produced by solid-state transformation during cooling from the high-temperature phase, austenite, and therefore, to refine the final microstructure (either the refinement of starting austenite or the increase of nucleation of ferrite or bainite in austenite if needed) (Refs. 27, 28). In the weld metal, it is difficult to achieve the refinement of austenite due to weld solidification, and, therefore, the latter choice — the increase of the nucleation of ferrite or bainite — has been attempted by dispersing nitride and/or oxide inclusions as heterogeneous nucleation sites in the weld metal (Refs. 27, 28). The solidification of low-alloy steel weld metals starts with primary ferrite, which changes to austenite by the peritectic reaction in the middle part of solidification. At the same time, the primary ferrite transforms to austenite. After solidification, the microstructure eventually becomes austenite single phase, which undergoes significant grain coarsening and ripening. Subsequent transformation takes place in the coarse austenite grains.

For the nucleation of ferrite and/or bainite in austenite of low-alloy steel welds, inclusions, such as TiN and titanium oxide (TiO), have been identified as effective nucleating agents (Refs. 27, 28). Both TiN and TiO are B1 compounds, having a sodium chloride crystal structure, and, thus, offer a low-energy coherent interface with bcc-Fe in the B-N orientation relationship at the nucleation of ferrite, as previously described (Ref. 24). There is a tendency that TiN works for the nucleation of ferrite at relatively high temperatures in
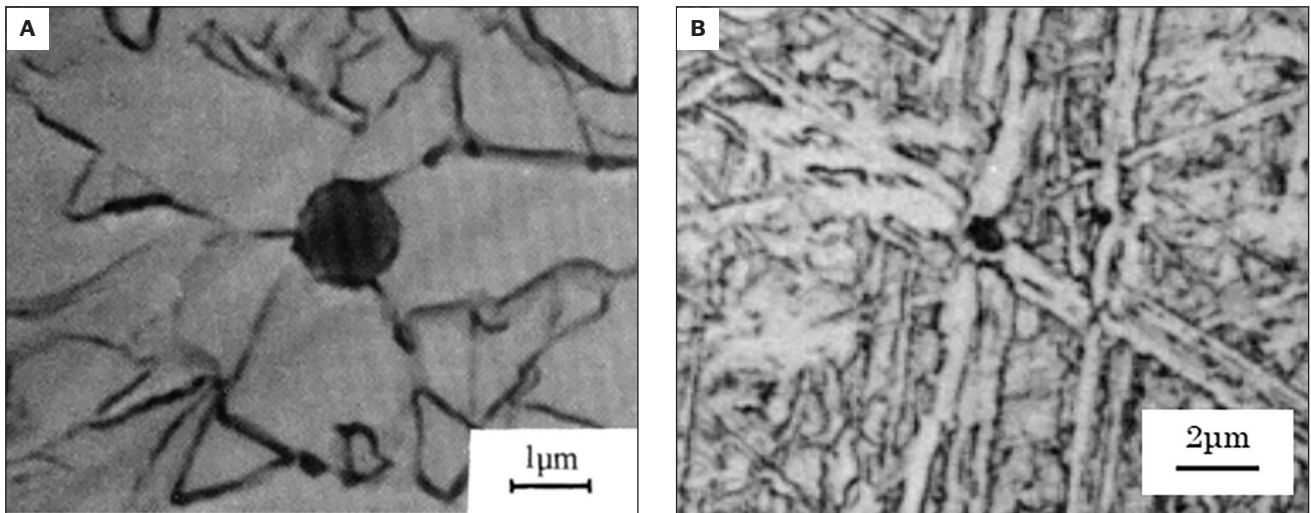
Fig. 17 — Intragranular ferrite nucleating on inclusions, nitrides, or oxides. A — Polygonal ferrite; B — acicular ferrite.
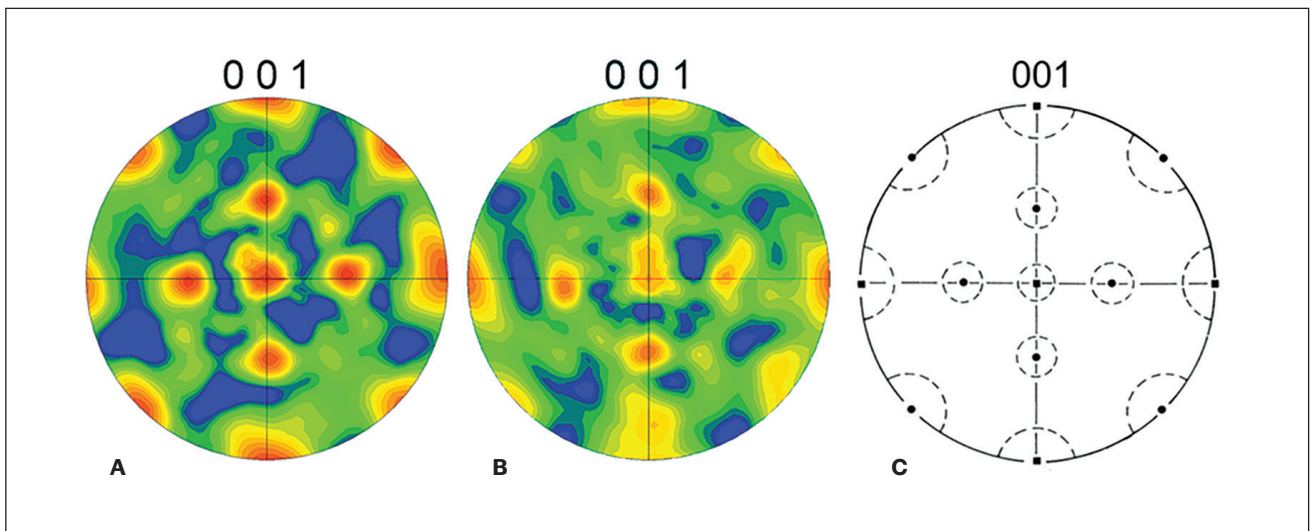

Fig. 18 — Orientation relationship between the embedded compounds and ferrite developed from the compounds: A — For TiN; B — for TiO; C — for the reference of B-N orientation relationship with an allowance of 5 deg misalignment to be compared with A and B (Ref. 31).

relatively low-carbon-equivalent (i.e., relatively low-strength) steel welds. The ferrite is often called polygonal ferrite due to its morphology; an example is shown in Fig. 17A. On the other hand, TiO is likely to encourage the nucleation of more bainitic ferrite at relatively low temperatures in relatively high-carbon-equivalent steel welds, where the ferrite produced is often called acicular ferrite due to its morphology; an example is shown in Fig. 17B. It was not clear why TiN and TiO showed different behaviors in ferrite formation, which became the motivation for our study. Also, when the ferrite formation becomes bainitic, such as Widmanstätten ferrite, the ferrite may need to have a low-energy orientation relationship with the mother phase, austenite, such as the Kurdjumov-Sachs (K-S) orientation relationship (Refs. 29, 30) as well as the B-N orientation relationship (Ref. 24) with TiO.

Before our study, whether the ferrite could satisfy both orientation relationships simultaneously had not been examined.

Single-crystal TiN and TiO were embedded in a low-alloy steel, and ferrite formation from the embedded compounds was examined in the steel after a welding thermal cycle with a peak temperature in the fully austenite region was given (Refs. 31, 32). Figure 18 (Ref. 31) shows the orientation relationship between the embedded compounds and ferrite developed from the compounds: A for TiN, B for TiO, and C for the reference of the B-N orientation relationship with an allowance of 5 deg misalignment with circles to be compared with A and B. Figure 18A was constructed by EBSD data from 53 ferrite grains, mostly polygonal, and Fig. 18B from 49 ferrite grains, mostly acicular. It was shown that ferrite grains generated from TiN and TiO have a B-N orientation relationship with the compounds, but it seems that ferrite
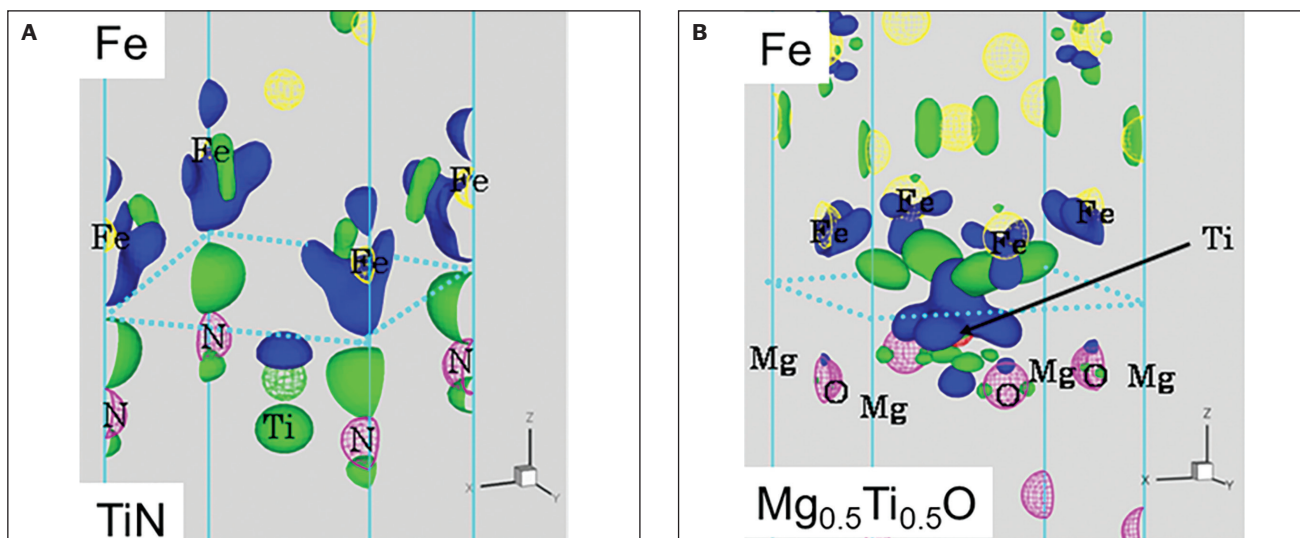
Fig. 19 — First principles calculation results showing differential charge density at the interfaces between bcc-Fe and B1 compounds: A — TiN; B — TiO with a B-N orientation relationship, $\{100\}_{bcc-Fe}$ //$\{100\}_{B1}$ and $<100>_{bcc-Fe}$ //$<110>_{B1}$. Note that for the calculation of the TiO-Fe interface, MgO was used as the base oxide for the stability of the calculation, and one Mg atom was replaced by the Ti atom (Ref. 31).
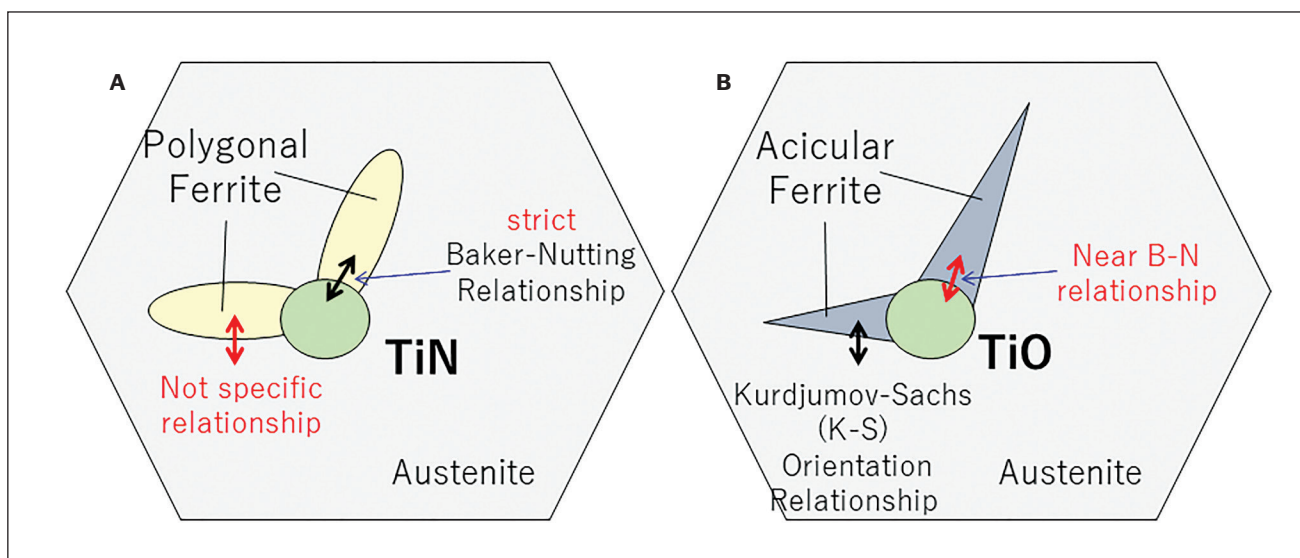

Fig. 20 — A schematic summary of intragranular ferrite formation in austenite. A — Polygonal ferrite on TiN; B — acicular ferrite on TiO.

from TiN shows a stricter B-N relationship than that from TiO. Ferrite grains from TiO show relatively larger misalignment from the B-N relationship. Examining orientation relationships between ferrite and prior austenite, it was found that ferrite from TiN did not show a specific relationship, while most of the acicular ferrite from TiO showed a K-S relationship. It was considered that ferrite from TiN can select a strict B-N relationship without the restriction of austenite, while ferrite from TiO needs to compromise in terms of a B-N relationship to satisfy the K-S relationship with the mother phase. Figure 19 (Ref. 31) shows the results of a first principles calculation showing differential charge density at the interfaces between bcc-Fe and B1 compounds, TiN and TiO,

with a B-N orientation relationship: $\{100\}_{bcc-Fe}$ //$\{100\}_{B1}$ and $<100>_{bcc-Fe}$//$<110>_{B1}$. In the figures, an increase in charge density is show in green and a decrease in blue. It is noted that in the calculation of the TiO-Fe interface, MgO was used as the base oxide, and one Mg atom was replaced by a Ti atom for the stability of the calculation. At the TiN-Fe interface, seen in Fig. 19A, there was not any significant charge interaction across the interface, and interfacial energy sharply increased with increasing misalignment from the B-N atom position. On the other hand, at the TiO-Fe interface, there was a charge interaction between Fe and Ti atoms. In Fig. 19B, charge density increased at the TiO-Fe interface, as indicated by the green areas, which suggests that Ti behaves like metal in TiO. This
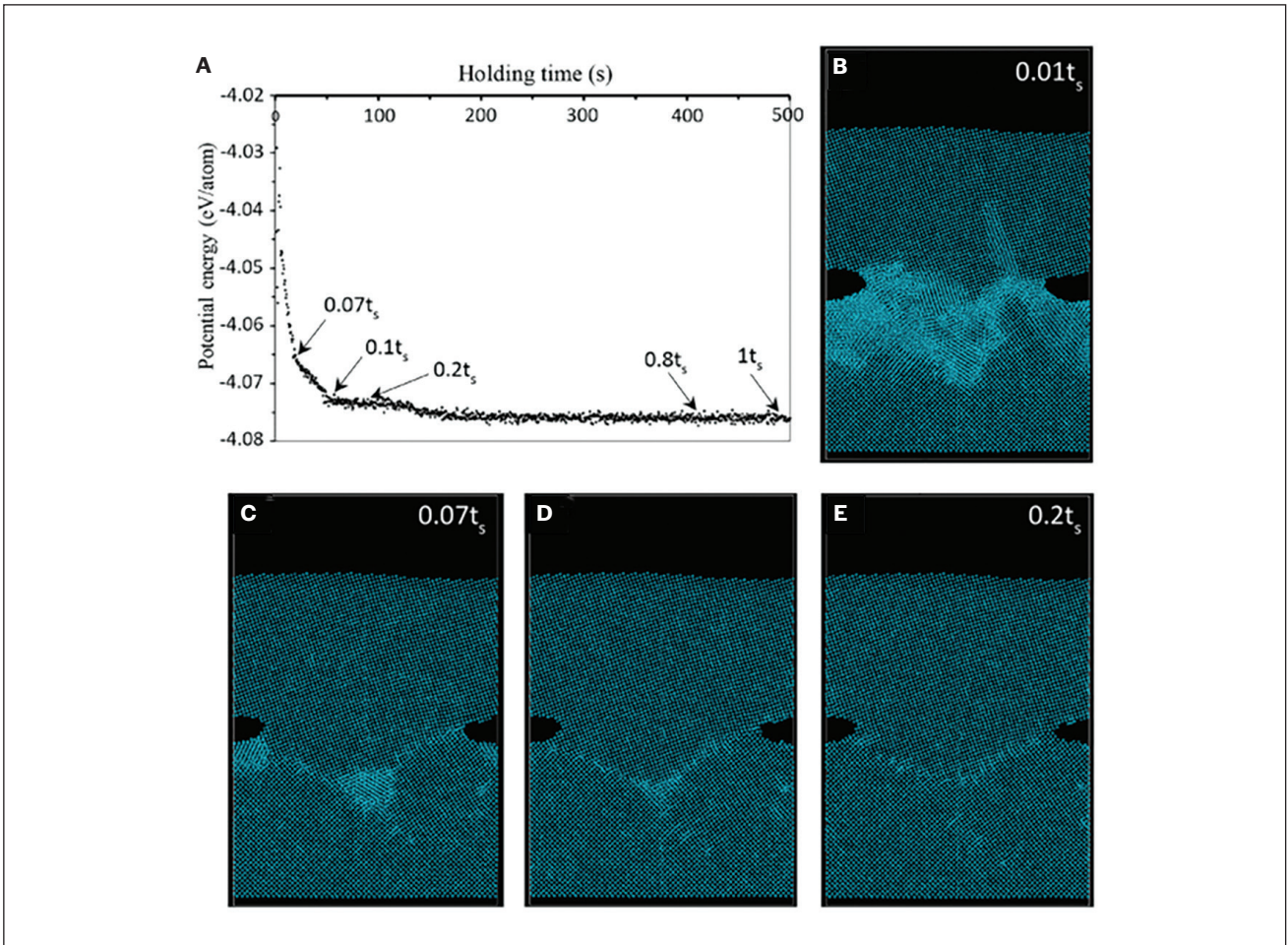
Fig. 21 — MD simulation of hot press for steel-steel bonding showing changes in the following: A — Total potential energy during isothermal holding; B–E — lattices annealed at 0.5 Tm after compression (Ref. 34).
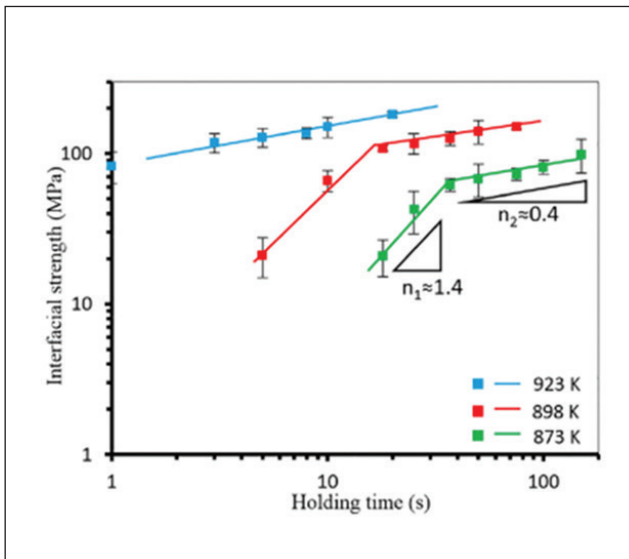

Fig. 22 — Evolution of interfacial strength under isothermal holding time after 5% compression for bonding (Ref. 34).

contributes to reducing interfacial energy in addition to a B-N relationship, and, thereby, some misalignment from the B-N atom position can be allowed for the low-energy interface.

Ferrite formation from B1 compounds is summarized in Fig. 20. Ferrite from TiN tends to have polygonal morphology, which is a product of diffusional transformation, and has a B-N orientation relationship with TiN without a specific orientation relationship with austenite, as shown in Fig. 20A. This indicates that the dispersion of TiN is more useful in relatively low-carbon-equivalent (i.e., relatively low-strength) steel welds and the HAZ, where the austenite-to-ferrite transformation temperature is relatively high. Ferrite from TiO, on the other hand, tends to have acicular morphology, indicating the product of relatively low-temperature transformation, and has both a B-N relationship with TiO and a K-S relationship with austenite. The difference from the ferrite from TiN is that a B-N relationship could be lax at the TiO-ferrite interface to concurrently satisfy the K-S relationship. Because of the characteristics, TiO dispersion, which has been successfully applied in various high-strength low-alloy steel weld metals, should be useful in relatively high-carbon-equivalent, high-strength steel weld metals.

Future Direction

As a future direction of welding and joining research, the author would like to repeat the importance of the use of various numerical simulations to understand complex welding behaviors and to better predict weld performance, although this importance has been recognized by many researchers and emphasized by many international conferences and seminars, such as Trends in Welding Research and Mathematical Modelling of Welding Phenomena. The author has applied the Monte Carlo simulation and first principles calculation in his research, as in some results shown in Figs. 14 and 19, as well as conventional finite difference and element methods (FDM and FEM) and the calculation of the phase diagram (CALPHAD) method. The Monte Carlo simulation method is quite useful for the modeling of microstructure development, grain growth, and other probabilistic behaviors during welding and joining, being combined with kinetic simulation of heat conduction, solute diffusion, and partitioning, etc., using the FDM. The combination of the FDM or FEM with the CALPHAD method is also useful because CALPHAD can supply thermodynamic information to kinetic simulation, such as phase stability, driving forces for transformation and diffusion, and two-phase equilibria for local equilibrium assumption. The author and his colleagues developed a numerical simulation model for weld solidification of multicomponent steels that combined the FDM for solidification kinetics and the CALPHAD software Thermo-Calc in the early 1990s (Ref. 33), which was the first attempt at this in welding research and was successfully applied to predict the weld solidification of different austenitic stainless steels.

As another important simulation method, the author and his colleagues employed a molecular dynamics (MD) calculation to understand interface development in the bonding and joining of steels and dissimilar metals (Refs. 34–36). Figure 21 (Ref. 34) shows a result of a MD calculation that was applied to hot press bonding of iron and iron, the calculation conditions of which were described elsewhere. It was seen that the lattice near the bonding interface was significantly distorted, but soon after, short-range rearrangement of atoms started under isothermal holding and nearly completed before the shrinkage of pores started by surface and boundary diffusion. This calculation accounts for the experimental result shown in Fig. 22 (Ref. 34), in which steel-to-steel hot press bonding was conducted and the evolution of bonding strength was measured as a function of isothermal holding time. A two-step increase in bonding strength was found, and it was considered that the first increase of strength resulted from the decrease of severe distortion near the bonding interface by short-range rearrangement of atoms, as the MD calculation suggests. In fact, both hardness measured by nano-indenter and Kernel Average Misorientation (KAM) values measured by EBSD near the bonding interface were found to decrease with time (Ref. 35), while the area of bonding interface did not increase during the first increase of bonding strength, all of which are consistent with the MD calculation and support the conclusion that the first increase was caused by the decrease of severe distortion near the surface. The second increase of the bonding interface with time was related to the observation of the increase of the bonded area resulting from the shrinkage of pores during isothermal holding, which was relatively slow compared with the first increase of strength due to the relatively long-range diffusion of atoms required for pore shrinkage. In summary, the use of the MD calculation was useful to understanding bonding behavior and interface formation and also helpful in interpreting the observation of the bonding experiment. Its application should be increased in future welding and bonding research.

It is important to note that multiphysics and multiscale simulations are needed to further increase the understanding of welding and joining behaviors because of their complexity. In other words, the integration of simulations of different physics and different scales will make it possible to predict properties and performances of welds and joints more correctly in future welding research. In the integration, experimental data can be connected to simulations to make each simulation better by data science techniques. The movement of the integration and connection of multiple simulations along with experimental data has already started in many areas, most actively in materials science areas. A noteworthy example is seen in PRISMS (Ref. 37), which is short for predictive integrated structural materials science and was started by the Materials Genome Initiative (MGI) under President Barack Obama's plan as a scientific platform that will enable accelerated predictive materials science for structural metals. The author also started a similar project in Japan under the Japanese government's financial support, which was called the Materials Integration (MI) project (Refs. 38, 39). In this project, different-scale simulations were collected and integrated in the MI system, while experimental data of materials from public and private sectors were collected and stored in the MI database to be applied to the simulations using data assimilation. The project is still continuing to expand the system and database, and an application of the system was attempted to predict weld performance of structural steels (Ref. 38). Also, there have been many similar research projects and research activities that focus on numerical modeling using different simulations.

In summary, the author believes that better understanding and control of welding and joining behaviors and performances of welds and joints would come from those projects and research activities. Also, it would be nice for young welding researchers and engineers to participate in those projects and activities and to make full use of the results.

References

1. Lippold, J. C., and Savage, W. F. 1979. Solidification of austenitic stainless steel weldments: Part I - A proposed mechanism. *Welding Journal* 58(12): 362-s to 374-s.

2. Lippold, J. C., and Savage, W. F. 1980. Solidification of austenitic stainless steel weldments: Part 2 — The effect of alloy composition on ferrite morphology. *Welding Journal* 59(2): 48-s to 58-s.

3. Lippold, J. C., and Savage, W. F. 1982. Solidification of austenitic stainless steel weldments: Part 3 — The effect of solidification behavior on hot-cracking susceptibility. *Welding Journal* 61(12): 388-s to 396-s.

4. Takalo, T., Suutala, N., and Moisio, T. 1979. Austenitic solidification mode in austenitic stainless steel welds. *Metallurgical Transactions A* 10A(8): 1173–1181.

5. Suutala, N., Takalo, T., and Moisio, T. 1980. Ferritic-austenitic solidification mode in austenitic stainless steel welds. *Metallurgical Transactions A* 11A(5): 717–725.

6. David, S. A. 1981. Ferrite morphology and variations in ferrite content in austenitic stainless steel welds. *Welding Journal* 60(4): 63-s to 71-s.

7. Kou, S., and Le, Y. 1982. The effect of quenching on the solidification structure and transformation behavior of stainless steel welds. *Metallurgical Transactions A* 13A: 1141–1152.

8. Lundin, C. D., DeLong, W. T., and Sponds, D. F. 1975. Ferrite-fissuring relationship in austenitic stainless steel weld metals. *Welding Journal* 54(8): 241-s to 246-s.

9. Brooks, P. S., and Lambert, F. J., Jr. 1978. The effect of phosphorus, sulfur and ferrite content on weld cracking of Type 309 stainless steel. *Welding Journal* 57(5): 139-s to 143-s.

10. Cieslak, M. J., Ritter, A. M., and Savage, F. 1982. Solidification cracking and analytical electron microscopy of austenitic stainless steel weld metals. *Welding Journal* 61(1): 1-s to 8-s.

11. Ogawa, T., and Koseki, T. 1988. Weldability of newly developed austenitic stainless alloys for cryogenic service: Part II – High-nitrogen stainless steel weld metal. *Welding Journal* 67(1): 8-s to 17-s.

12. Brooks, J. A., and Thompson, A. W. 1991. Microstructural development and solidification cracking susceptibility of austenitic stainless steel welds. *International Materials Reviews* 36(1): 16–44.

13. Brooks, J. A., Williams, J. C., and Thompson, A. W. 1983. Microstructural origin of the skeletal ferrite morphology of austenitic stainless steel welds. *Metallurgical Transactions A* 14A(6): 1271–1281.

14. Kujanpaa, V., Suutala, N., Takalo, T., and Moisio, T. 1979. Correlation between solidification cracking and microstructure in austenitic and austenitic-ferritic stainless steel welds. *Welding Research International* 9(2): 55–76.

15. Inoue, H., Koseki, T., Ohkita, S., and Fuji, M. 2000. Formation mechanism of vermicular and lacy ferrite in austenitic stainless steel weld metals. *Science and Technology of Welding and Joining* 5: 385–396.

16. Inoue, H., and Koseki, T. 2017. Solidification mechanism of austenitic stainless steels solidified with primary ferrite. *Acta Materialia* 124: 430–436.

17. Westin, E. M. 2022. Hot cracking in duplex stainless steel weldments – A review. *Welding in the World* 66: 1483–1499.

18. Koseki, T. 1989. Unpublished data.

19. Suutala, N., Takalo, T., and Moisio, T. 1979. Single-phase ferritic solidification mode in austenitic-ferritic stainless steel welds. *Metallurgical Transactions A* 10A(8): 1183–1190.

20. Ogawa, T., and Koseki, T. 1989. Effect of composition profiles on metallurgy and corrosion behavior of duplex stainless steel weld metals. *Welding Journal* 68(5): 181-s to 191-s.

21. Villafuerte, J. C., Pardo, E., and Kerr, H. W. 1990. The effect of alloy composition and welding conditions on columnar-equiaxed transitions in ferritic stainless steel gas-tungsten arc welds. *Metallurgical Transactions A* 21A: 2009–2019.

22. Koseki, T., and Inoue, T. 2001. Equiaxed solidification of steel nucleating on titanium nitride. *Journal of the Japan Institute of Metals* 65(7): 644–651.

23. Koseki, T., Inoue, H., Fukuda, Y., and Nogami, N. 2003. Numerical simulation of equiaxed grain formation in weld solidification. *Science and Technology of Advanced Materials* 4(2): 183–195.

24. Bramfitt, B. L. 1970. The effect of carbide and nitride additions on the heterogeneous nucleation behavior of liquid iron. *Metallurgical Transactions* 1: 1987–1995.

25. Sundman, B., Jansson, B., and Andersson, J.-O. 1985. The Thermo-Calc databank system. *CALPHAD* 9(2): 153–190.

26. Gäumann, M., and Kurz, W. 1998. Why is it so difficult to produce an equiaxed microstructure during welding? In *Mathematical Modelling of Weld Phenomena 4*, edited by Cerjak, H., 125–136. London: IOM.

27. Koseki, T. 2005. A review on inclusion-assisted microstructure control in C-Mn and low alloy steel welds. *Welding in The World* 49: 22–28.

28. Koseki, T., and Thewlis, T. 2005. Inclusion assisted microstructure control in C-Mn and low alloy steel welds. *Materials Science & Technology* 21: 867–879.

29. Kurdjumov, G., and Sachs, G. 1930. On the mechanism of hardening of steel. *Z. Physik.* 64: 325–343.

30. Yardley, V. A., and Payton, E. A. 2014. Austenite-martensite/bainite orientation relationship: Characterization parameters and their application. *Materials Science and Technology* 30(9): 1125–1130.

31. Kasai, K., Lee, C., Nambu, S., Inoue, J., and Koseki, T. 2010. Transformation behavior of ferrite at steel/B1 compounds interface. *Tetsu-to-Hagané* 96(3): 123–128.

32. Lee, C., Nambu, S., Inoue, J., and Koseki, T. 2011. Ferrite formation behaviors from B1 compounds in steels. *ISIJ International* 51(12): 2036–2041.

33. Koseki, T., Matsumiya, T., Yamada W., and Ogawa, T. 1994. Numerical modeling of solidification and subsequent transformation of Fe-Cr-Ni Alloys. *Metallurgical & Material Transactions A* 25A: 1309–1321.

34. Pongmorakot, K., Nambu, S., Shibuta, Y., and Koseki, T. 2017. Investigation on the mechanism of steel/steel solid-state bonding at low temperatures. *Science and Technology of Welding and Joining* 22(3): 257–263.

35. Pongmorakot, K., Nambu, S., Shibuta, Y., and Koseki, T. 2018. Effects of compressive strain on the evolution of interfacial strength of steel/nickel solid-state bonding at low temperature. *Science and Technology of Welding and Joining* 23(4): 344–350.

36. Pongmorakot, K., Nambu, S., and Koseki, T. 2018. Numerical analysis of effects of compressive strain on the evolution of interfacial strength of steel/nickel solid-state bonding. *Materials Transactions* 59(4): 568–574.

37. PRISMS, Electronic References. Retrieved August 14, 2023, from *prisms-center.org/#/home*.

38. Demura, M., and Koseki, T. 2020. SIP – materials integration project. *Materials Transactions* 61(11): 2041–3046.

39. National Institute for Materials Science. Materials Data Platform. *nims.go.jp/eng/research/platform/materials-data*

TOSHIHIKO KOSEKI (*koseki.toshihiko@kuas.ac.jp*) is formerly with the University of Tokyo and currently with the Kyoto University of Advanced Science, Kyoto, Japan.